ADA044664

Project Report

LRP-5

B. A. Francis

Analysis of Firepond IR RCS Data
on Rocket Model

18 May 1977

Lincoln Laboratory

MASSACHUSETTS INSTITUTE OF TECHNOLOGY

LEXINGTON, MASSACHUSETTS

D D C

SEP 14 1977

B

This technical report has been reviewed and is approved for publication.

FOR THE COMMANDER
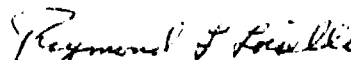
Raymond L. Loiselle, Lt. Col., USAF
Chief, ESD Lincoln Laboratory Project Office

MASSACHUSETTS INSTITUTE OF TECHNOLOGY

LINCOLN LABORATORY

ANALYSIS OF FIREPOND IR RCS DATA
ON ROCKET MODEL

B. A. FRANCIS (RCA)

Group 37

PROJECT REPORT LRP-5

18 MAY 1977

D D C

SEP 1⊿ 1977

B
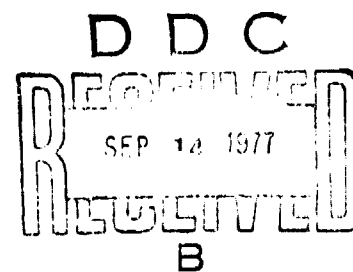
LEXINGTON   MASSACHUSETTS

ABSTRACT

Coherent narrowband infrared radar returns from a rotating target mounted on a fixed pedestal were analyzed. The data were recorded using the Firepond radar facility with small-aperture transmitting and receiving antennas, the target was located at a range of 5 km. The amplitude distributions of the target returns were compared with those from a spherical mirror.

CONTENTS

I. INTRODUCTION

The Firepond infrared radar is a 10.6-μm wavelength monostatic radar that, in its normal configuration, radiates and receives via a 48-in.-dia. steerable antenna. When observing targets at long range, the transmission usually consists of a constant-frequency pulse of 4-msec duration, with a pulse repetition period of 16 msec. This duty cycle of one in four allows the returns to be received with the same antenna, during the transmit interpulse interval, and to be separated from the transmitted signal by a rotating multiplexer disk. This technique cannot be used for measurement on models at short range (say 5 km), because of the short time delay between transmission and reception. For short range measurements, a bistatic radar configuration is preferred since the transmit and receive paths are separate and require no multiplexing. Such a bistatic system was set up at the Firepond facility and used on several occasions to record the returns from models.

A. Radar Configuration

The configuration of the radar transmitting and receiving systems for these measurements was as follows: The output of the 1-kW transmitter amplifier (operating at reduced power) was directed, via a series of flat mirrors, up to the top of the Firepond antenna tower and from there to the target at a range of 5 km. The returned signal was similarly transferred, via a separate set of mirrors, from the top of the tower to the receiver IR coherent detector. The only lens in the system was associated with the detector. The diameter of the transmitted beam was approximately 5 cm.

For a beam of uniform intensity, the half-power beamwidth would be 0.22 mrad, giving a beam diameter of 1.1 m at a range of 5 km. The power in the actual beam was concentrated toward the center, so the actual diameter at the target was probably 1.5 to 2.0 times this figure. This beam was comparable with the size of the target, so some variation in field strength over the target was expected. The transmitted beam was linearly polarized, and the detector was polarization sensitive and was adjusted for maximum sensitivity on the return from a corner reflector.

The transmission was continuous and the received signal was coherently detected, digitized, and recorded. The sampling rate, and the number of contiguous samples processed, were determined by the Doppler spread expected in the particular test and the Doppler resolution desired.

Although the radar configuration was bistatic, the distance of approximately 1 m between the transmitting and receiving ports was small compared to the 5-km range to the target, hence the analysis of the returns was performed as if the radar had been monostatic.

B. Target Characteristics

The target used for the experiments reported here was a scale model of a rocket body with re-entry vehicle attached. Figure 1 is an outline drawing with dimensions, and Fig. 2 is a photograph of the model. The model differed from the drawing in that only one of the vernier motors and one of the translation motors were present. The vernier motor was mounted inside the rear end of the cylinder and protruded beyond the rear edge. The RV model appears to have been fabricated from aluminum alloy plate and finished by machining on a lathe. The surface roughness on the RV model was approximately 1 to 2 μm for the spherical nose and 3 to 4 μm for the conical section. The foremost conical section of the rocket body model was also turned and had a surface roughness somewhat in excess of 5 μm. The remainder of the body did not show

1
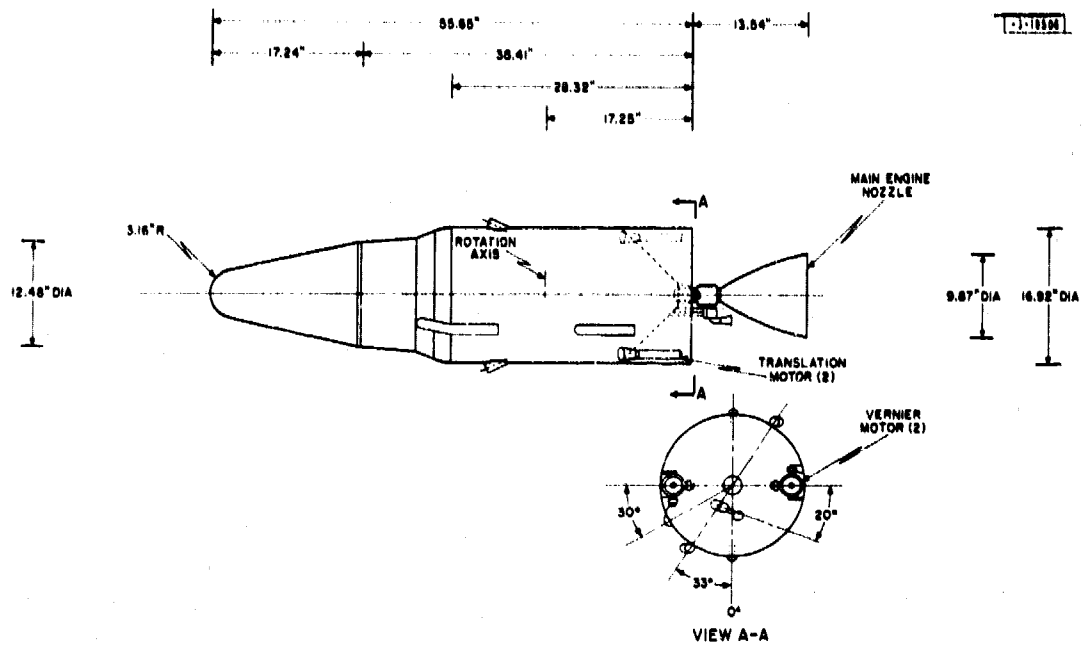
Fig. 1. Outline drawing of model.

P160-850

Fig. 2. Photograph of model.

2

machining marks but appeared to have been thoroughly abraided with fine abrasive paper. The main engine nozzle had been turned with a roughness in excess of 5 µm.

Since the materials used in the construction of the model, and the surface finish obtained, were different from those of the full-size object, no inferences have been drawn from this analysis regarding the possible returns from the full-size object.

The model was mounted on two vertical supports with the translator motor in the same horizontal plane as the body axis. The supports were attached to a turntable which was rotated about a vertical axis at a uniform velocity. The direction of rotation was clockwise from the top, and the radar line of sight (RLOS) was approximately horizontal.

II. ROTATING MODEL EXPERIMENT 22 OCTOBER 1976

A. Returns from the Body

Figure 3 shows a Doppler-Time-Intensity (DTI) display of the Doppler spectrum of the returns from the model. These data were recorded on 22 October 1976 (day 296). The rotation rate of the turntable was 2 rpm, the sampling interval was 10 µsec, and groups of 800 samples were taken at a spacing of 32 msec. This gave a Doppler resolution of 170 Hz with Hamming weighting, equivalent to a cross-range resolution of 8.6 mm. The longitudinal lines drawn on the DTI were generated by a simulation program and represent the expected Doppler frequencies of a number of body features. At the bottom of Fig. 3, starting from the left, these lines represent in order, the point of reflection on the nose sphere, the junction of the nose sphere and the RV cone, the junction of the RV and the first cone on the body, the junction of the first and second body cones, the junction of the second cone and the cylinder, the end of the cylinder, and the rear edge of the nozzle. As the model passed through the zero aspect position (nose towards radar), the nose return persisted while other returns desappeared to reappear on the other side. The shielding of the body features was simulated to a limited extent in the simulation program.

After zero aspect, lines corresponding to two additional discrete scatterers on the side of the cylinder are shown. These represent the nozzle of the translator motor and the front end of a cable duct. A weak consistent return can be seen to the right of the simulated translator motor return; this misalignment indicates a small error in the placement of this feature. A weaker return is coincident with the cable duct line. The transverse lines on this figure represent the positions of the cylindrical and conic surfaces when they are perpendicular to the RLOS. Features not modeled in the simulation are the zero-frequency return from the mount and surrounding objects and the supporting strut whose return is visible to the right of center in the lower part of Fig. 3.

The DTI is characterized chiefly by the identifiable surface returns. The cylinder surface gave a return which was generally low in amplitude except in the region from 8 deg before the broadside position to 8 deg after. The amplitude of the returns from each of the three cones passed through a maximum when their surfaces were perpendicular to the RLOS but each also showed some degree of asymmetry. Note that discrete returns were not generated by the junctions of these sections.

B. Returns from the Spherical Nose

Figure 4 is a DTI of the data taken on 12 November 1976, with compensation made for the motion of the spherical nose. This compensation had the effect of making the nose return
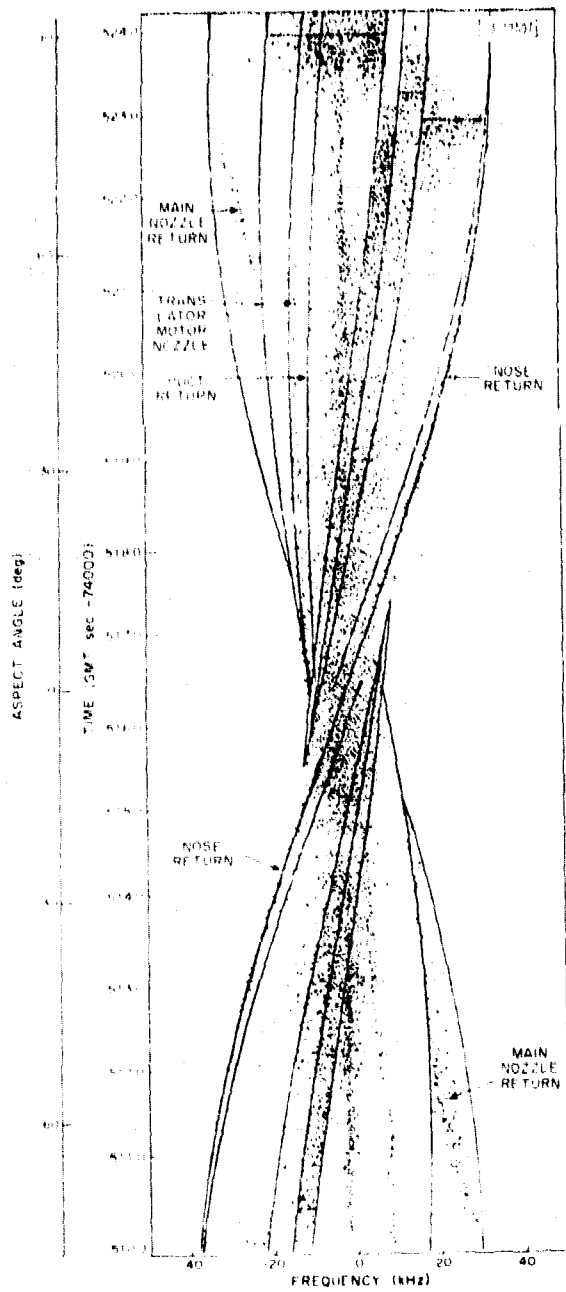
Fig. 5.   DTI of rotating model, 22 October 1976.

4
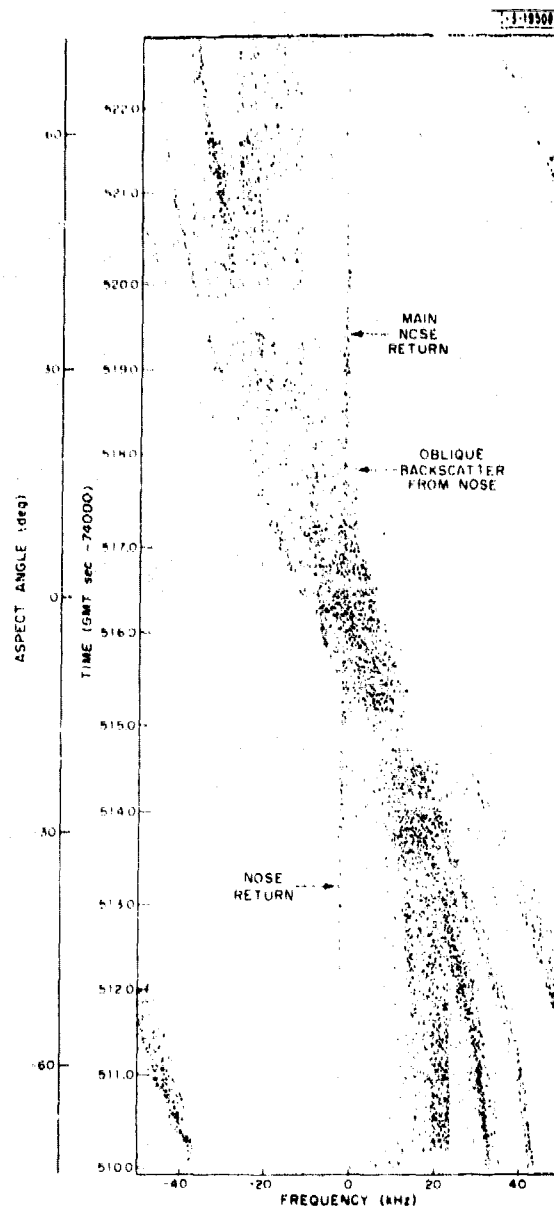
Fig. 4. DTI of rotating model, tracked nose return, 22 October 1976.

stationary in Doppler frequency. The return from the nose can be seen clearly at a Doppler frequency of 4 kHz. Immediately before and after the time when the object is in the zero aspect position (approximately 74516 sec), weak returns can be seen to the side of, and running parallel to, the principal nose return. These are apparently returns from the sperical surface at very oblique incidence and are due possibly to specular returns from the machining marks, or to the machining marks acting as a diffraction grating.

Figure 5 shows the amplitudes of the Doppler spectra of the signal. It can be seen that the spectrum of the tracked nose return is at times as broad as 2 kHz and that the peak of the return moves within this range. It should be noted that the theoretical Doppler spread over the diameter of the sphere is 6.3 kHz, whereas the observed spread is approximately 2 kHz. This indicates that most of the energy is returned from an area approximately one-third the diameter of the sphere. Note however, that these data did not include the returns from the full diameter of the sphere seen near zero aspect.

C. Peak Nose Returns

Figure 6 shows the amplitude of the nose return as a function of time. These data represent the maximum signal within the Doppler range of the return. The large return in the vicinity of zero aspect is due to other body features passing through the Doppler cells occupied by the nose return. To avoid this interference, the data were separated into two time intervals, one before and one after the interference. These intervals were then analyzed separately.

It can be seen from the amplitude plots that the nose return has three distinguishable components. These are (1) a low-frequency component that is symmetrical about the zero aspect position at 74516.5 sec, (2) a linear component that increases about 5 dB over the time span, and (3) a high-frequency component. The symmetrical component is largely due to the variation of the surface characteristics of the sphere. This sphere was machined by turning in a lathe and therefore has symmetrical characteristics. The slowly changing linear component is probably due to nonuniform illumination. The high-frequency component could be due to combination of the target surface, the atmosphere, and the radar characteristics. One of the objectives of this analysis was to distinguish between these effects.

D. High-Frequency Component of the Nose Return

The high-frequency component of the nose return was extracted by processing the signal in a low-pass digital filter to obtain the zero- and low-frequency components, and then subtracting these from the signal to leave only the high frequencies.

The amplitude and phase error characteristics of the three-pole low-pass filter used are shown in Fig. 7. The phase slope of the filter at zero frequency was equivalent to a delay of 20 samples. From the figure, it can be seen that the 3-dB attenuation frequency is approximately 0.016/T, where T is the time between samples applied to the filter. In this specific test, T was 0.032 sec, making the 3-dB frequency 0.5 Hz.

The various factors affecting the signal amplitude acted in a multiplicative fashion, that is, the amplitude of the return was proportional to the product of various terms that were functions of the target RCS, the atmospheric attenuation, the illumination power density, the receiver gain, etc. In removing the slowly varying components with the low-pass filter, the signal was first converted to decibels so that the subtraction of the low-frequency components was, in effect, a division. This preserved the characteristics of the high-frequency component.

6
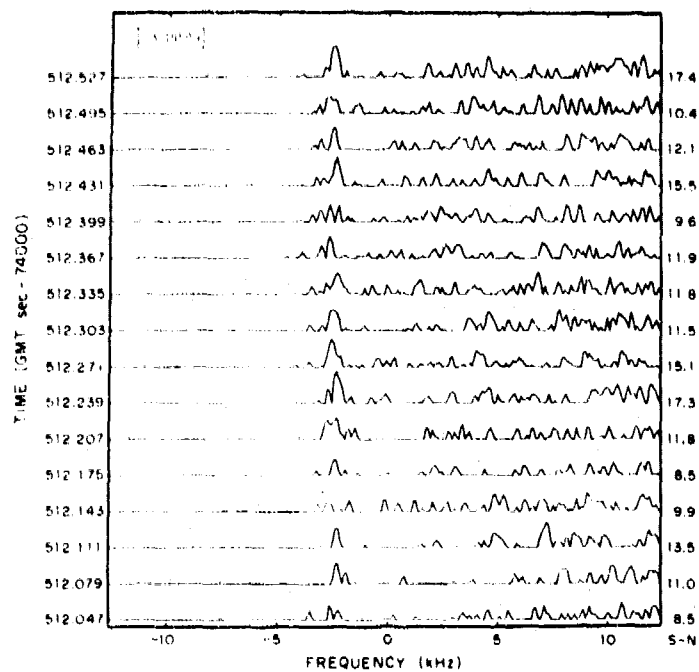
Fig. 5. Amplitude of Doppler spectrum, rotating model, 22 October 1976.
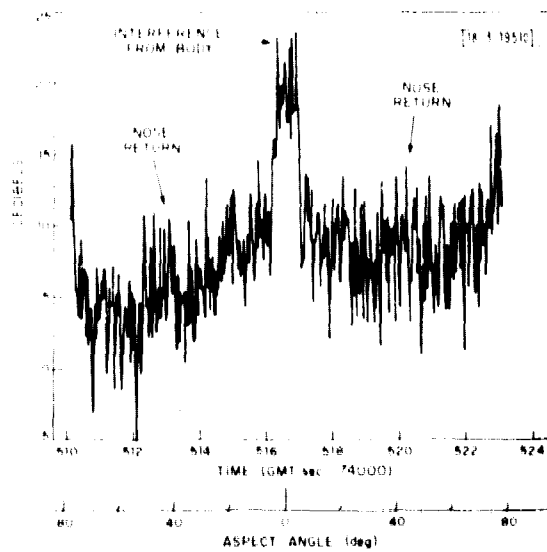
Fig. 6. Peak nose return vs time, 22 October 1976.
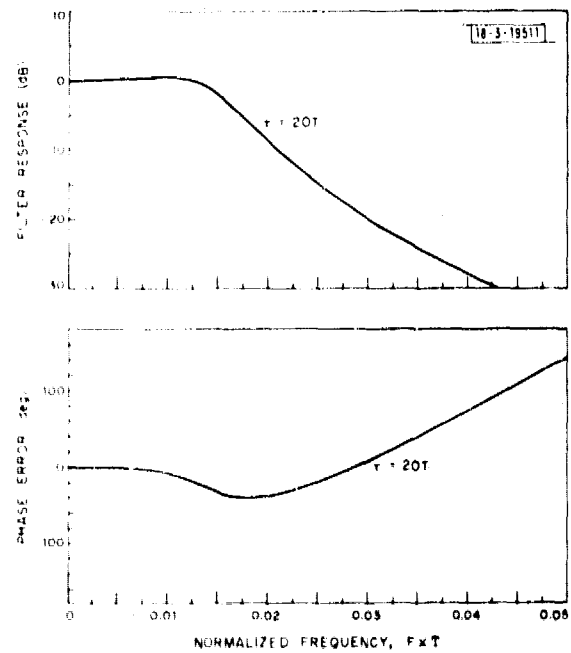
Fig. 7. Frequency response of low-pass digital filter.

Figures 8 and 9 relate to the nose return in the time interval before zero aspect. The upper section of Fig. 8 shows the amplitude of the unmodified return. This is similar to the left-hand section of Fig. 6 plotted to a different time scale. The center section of Fig. 8 shows the low-frequency component as extracted by the low-pass filter, and the lower section shows the high-frequency component left after subtracting the low frequencies. Figure 9 shows the histogram of the amplitude of the high-frequency component and the cumulative amplitude distribution. The signal amplitude has a mean of zero (since the zero-frequency component has been removed by the filter) and a standard deviation of 2.6 dB. The distribution is approximately symmetrical about zero.

Similar plots for the nose return in the time period after zero aspect showed a standard deviation of 2.8 dB; the distribution was less symmetrical, being biased toward the lower amplitude.

E. Single-Cell Return from Nose

The amplitude of the signal discussed in the preceding section was derived by taking the maximum within a range of Doppler cells. This did not give a direct indication of the character-istics of the signal within each cell. If the surface of the nose was rough compared to a wave-length, the return in a single cell would be composed of the returns from many independently phased scatterers. The signal would then be expected to have the characteristics of narrowband noise and would have a Rayleigh amplitude distribution. In this section, the signals discussed were obtained from the single Doppler cell that gave the highest average return. These were filtered and analyzed as before. Data from the two time segments were treated independently. Figures 10 and 11 show the signal components and amplitude distributions for the first time segment. The mean signal level is now 6 dB lower than the corresponding peak signal, and the standard deviation has increased from 2.6 to 5.5 dB. In the second time segment, the mean signal dropped by 7 dB and the standard deviation increased from 2.8 to 6.4 dB.

F. Comparison with Noise Signal

To determine if the high-frequency component of the signal amplitude had the character-istics of noise, a Rayleigh distributed signal was generated from pseudorandom noise and processed in the same manner as the nose return. A section of the amplitude history is shown in Fig. 12, and the amplitude histogram and cumulative distribution in Fig. 13. The standard deviation for this signal is 6.2 dB. This amplitude distribution and standard deviation show a good match to those of the single-cell nose returns, indicating that the nose returns had sub-stantially Rayleigh distribution.

G. Returns from the Rocket Nozzle

Apart from the nose return, the most clearly defined return came from the nozzle at the rear of the body. Figure 14 is a DTI with compensation for the motion of the nozzle. This compensation made the rear edge of the nozzle stationary in doppler. Near the beginning and end of the record, the maximum signal came from surfaces that were perpendicular to the RLOS, but in the range of aspect angle 45 deg either side of zero aspect, the rear of the cylinder shielded these parts of the nozzle. Within this range, the returns were more diffuse since they were backscattered at an oblique angle. Because of the larger radius of curvature, the nozzle gave a broader spectrum of diffuse returns than the nose. The amplitude of the return is shown

8

Fig. 8. Components of peak nose
return, 22 October 1976.

DECIBLES

TIME (GMT sec -74000)

18-5-19513

NUMBER OF OCCURRENCES
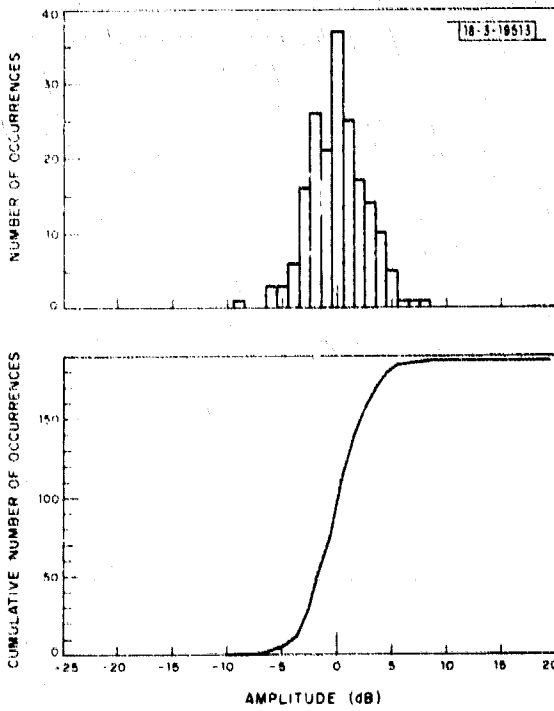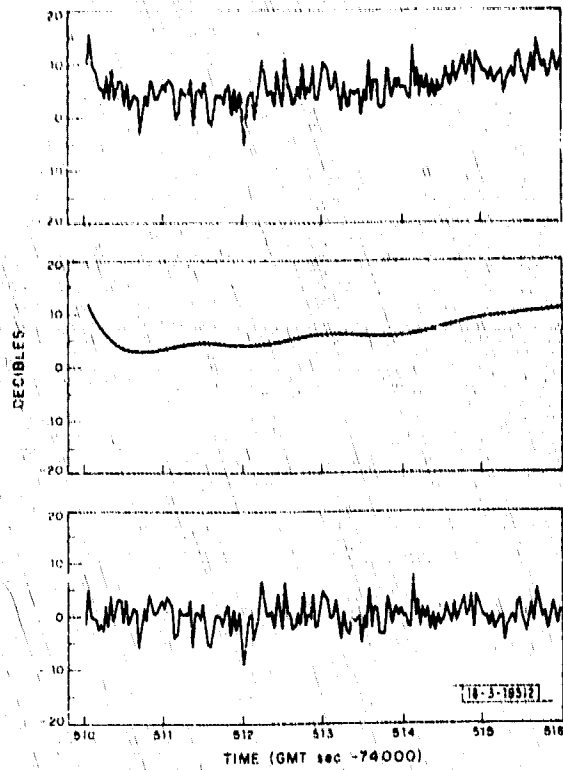
Fig. 9. Amplitude distribution of peak
nose return, 22 October 1976.

CUMULATIVE NUMBER OF OCCURRENCES

AMPLITUDE (dB)

9
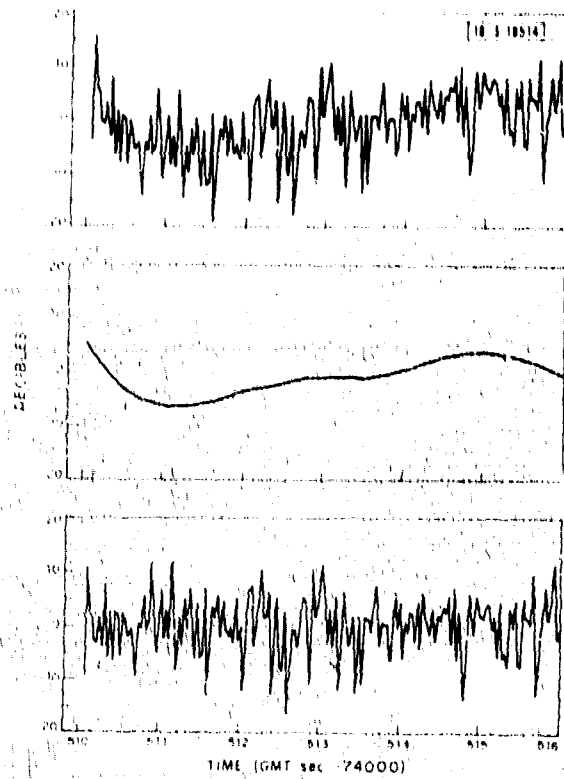
Fig. 10.   Components of single-cell nose return, 22 October 1976.


Fig. 11.   Amplitude distribution of single nose return, 22 October 1976.

10
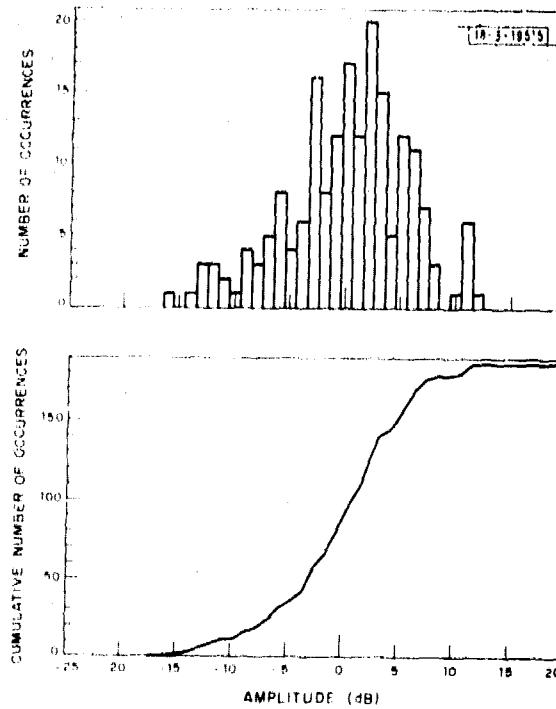
Fig. 12.   Noise signal amplitude vs time.
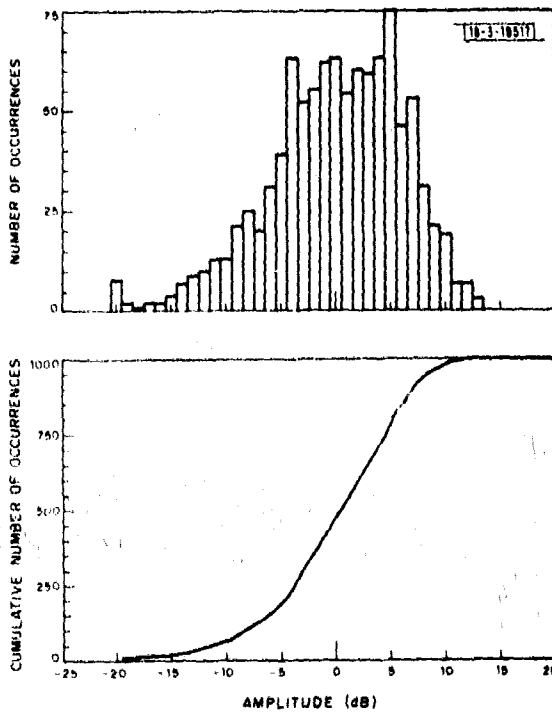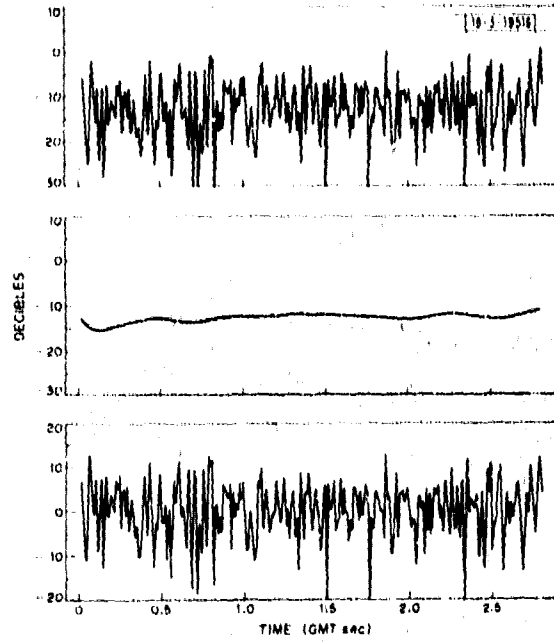
Fig. 13.   Amplitude distribution of noise signal.
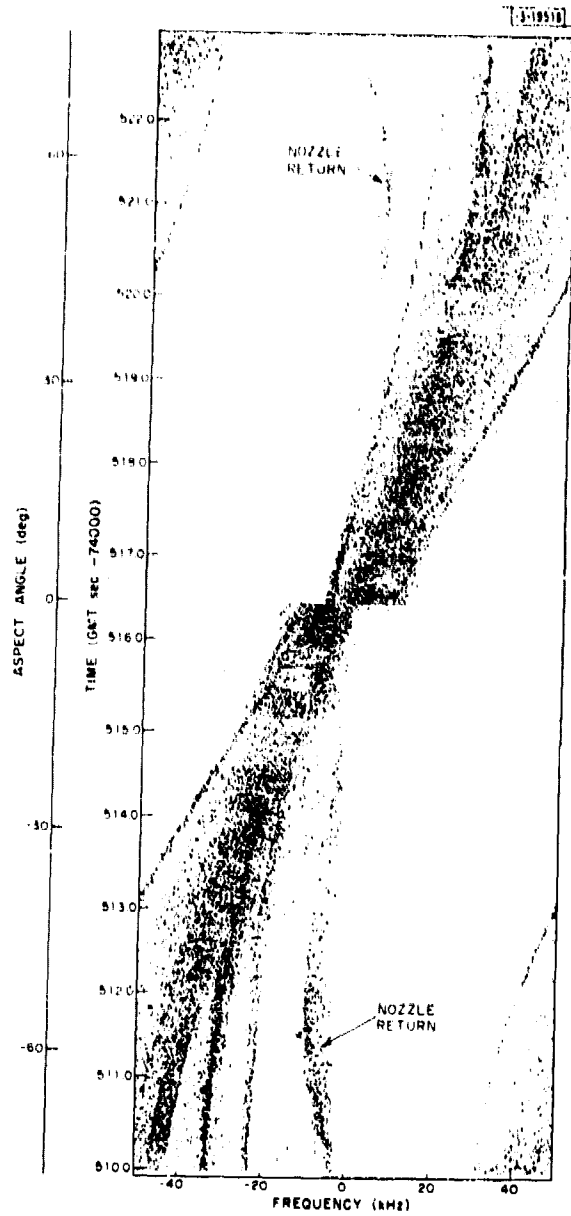
Fig. 14.   DTI of rotating model, tracked nozzle return,
22 October 1976.

12

as a function of time in Fig. 15. This amplitude is the maximum within the range of Doppler cells containing the nozzle return. Since the nozzle returns were not present near zero aspect, the signals were separated into two time intervals and processed separately in the same manner as the nose return. The amplitude histories and histograms for the first section are shown in Figs. 16 and 17. The standard deviation, after removal of the low frequencies, was 2.0 dB. The corresponding standard deviation for the second section was 2.4 dB. The distributions were approximately symmetrical on a decibel scale.

III. FIVE-KM RANGE EXPERIMENT 16 NOVEMBER 1976

A. Introduction

The rotating-model experiments described above were repeated on 16 November 1976. In addition to the model, a concave spherical mirror with a radius of curvature of 1 m was mounted on the turntable. This was positioned alongside the nose and faced forward. The model was rotated at a rate of 1 rpm with groups of 400 samples being taken with a sample spacing of 20 μsec and a group spacing of 32 msec. This gave a Doppler resolution of 170 Hz with Hamming weighting. This corresponded to a cross-range resolution of 8.6 mm. Figure 18 shows the DTI of the model returns. This DTI is similar to that for the previous data except for the strong mirror return, and the smaller returns from the mirror mounting. After the object passed through the zero aspect position, the mirror mounting returns became confused with the nose return. This prevented a clean nose return from being extracted. Because of this difficulty, the nose returns after the zero aspect position were not processed. The mirror return was stronger than the other returns and was approximately 10 dB greater than the zero-frequency returns from the stationary surroundings.

B. Returns from the Spherical Nose

Figure 19 is the DTI corrected for the motion of the nose, while Fig. 20 gives a sample of the amplitude display of the Doppler spectra. These single-cell and peak signals were analyzed as for the earlier experiment. The standard deviation for the peak signal was 2.7 dB and for the single Doppler cell was 6.0 dB. The amplitude distribution was symmetrical for the peak signal and was similar to that for the Rayleigh distribution for the single-cell signal.

C. Returns from the Spherical Mirror

Figure 21 is a section of the DTI of Fig. 18 with compensation for the motion of the mirror. Figure 22 is a sample of the amplitude displays of the Doppler spectra. It is obvious that the mirror returns are stronger and are steadier in both amplitude and frequency than the nose returns. There are, however, some small variations in frequency that are probably due to changes in the rate or rotation. The plots of peak signal amplitude (maximum in Doppler frequency space) in Figs. 23 and 24 show the signal to have an amplitude of 30 dB and a high-frequency component of 0.8 dB standard deviation. The absolute RCS of a specular spherical surface is equal to the area of a circle whose radius is the radius of curvature of the surface. The RCS of the mirror with 1-m radius of curvature is therefore 3.14 m^2 or 5.0 dBsm.

The signal in the Doppler cell that gave the highest average return was analyzed as before. The standard deviation of the high-frequency component in the single cell was found to be 3.2 dB, the increase from 0.8 dB being due to variations in frequency of the peak return.

13
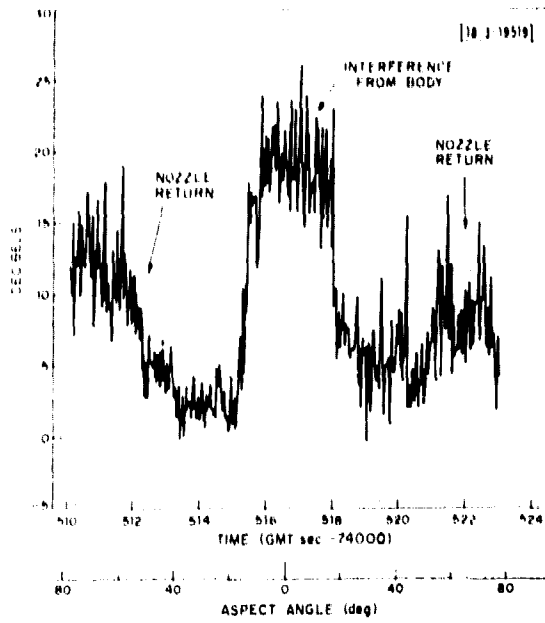
Fig. 15. Peak nozzle return vs time, 22 October 1976.
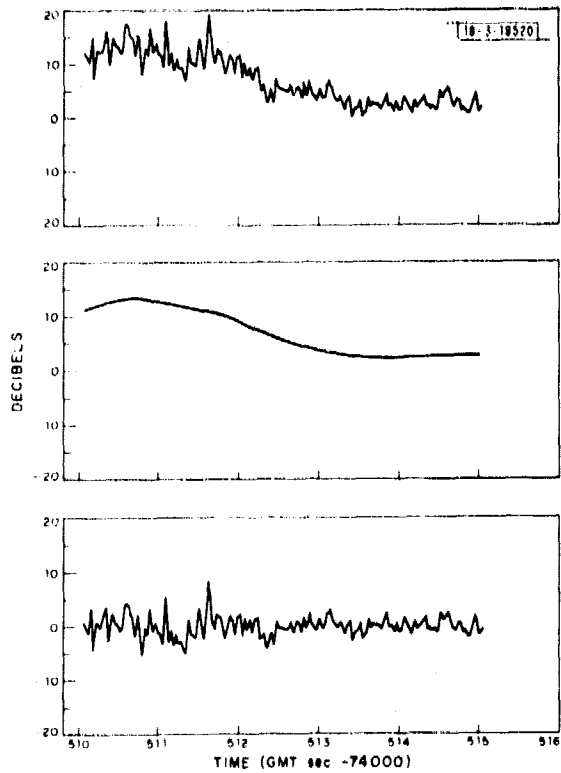
Fig. 16. Components of peak nozzle return, 22 October 1976.
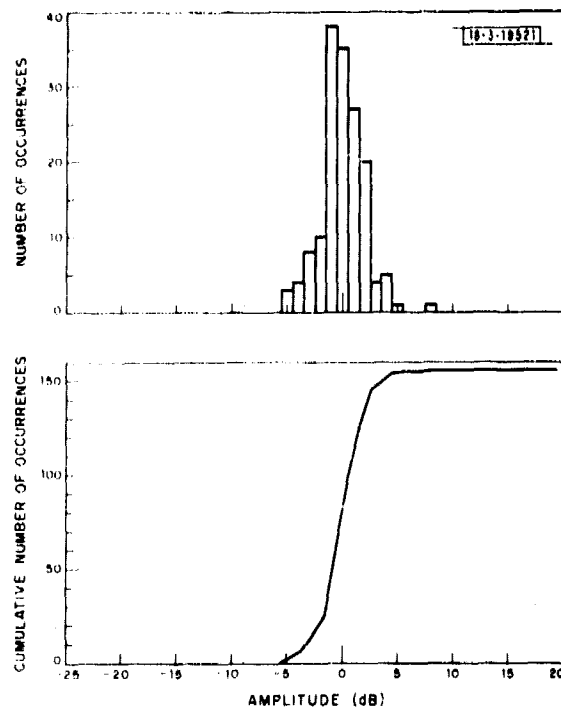
Fig. 17. Amplitude distribution of peak nozzle return, 22 October 1976.
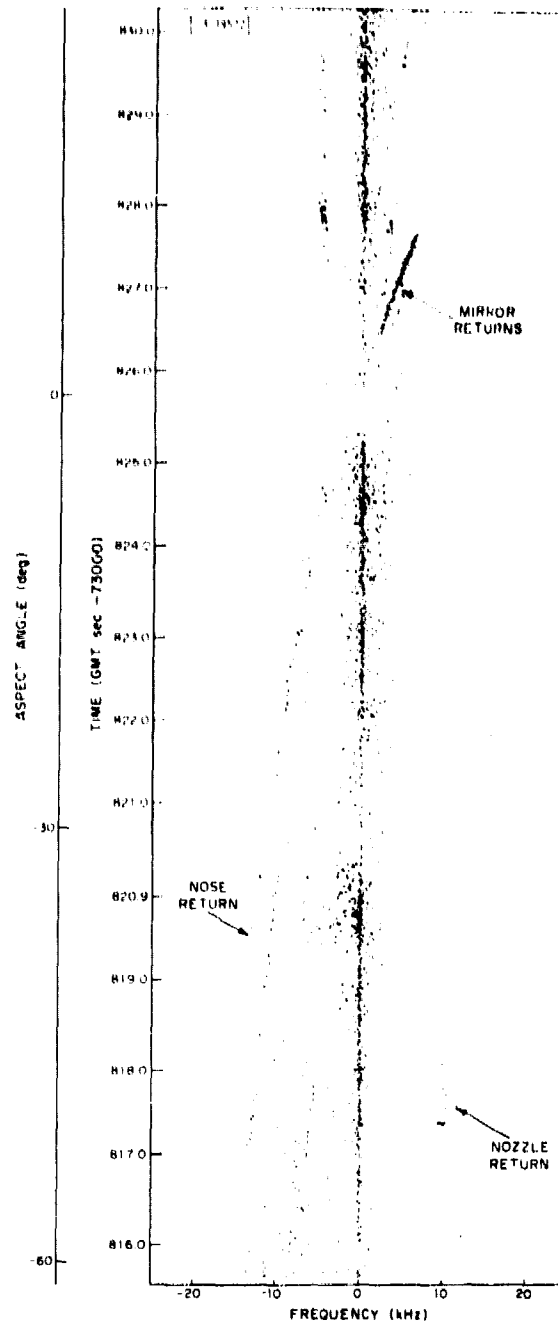
Fig. 18. DTI of rotating model with mirror, 16 November 1976.

15
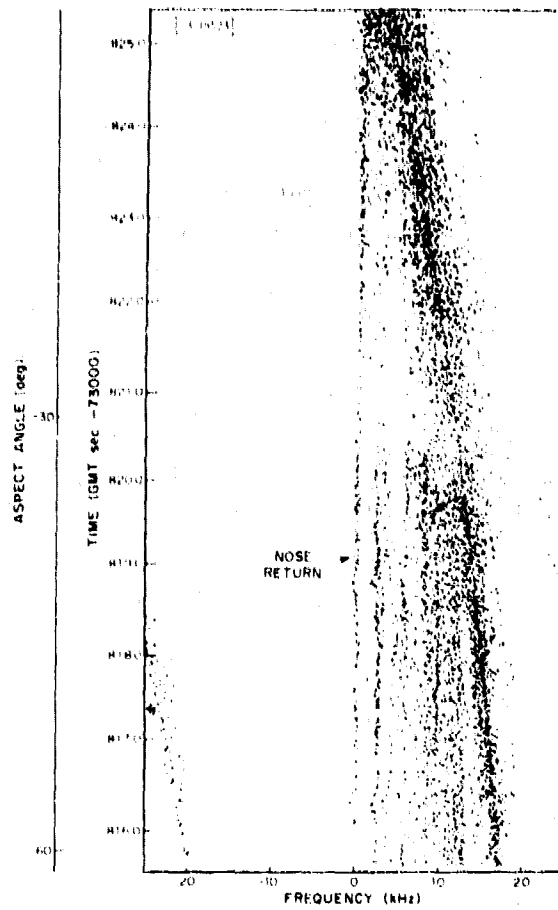
Fig. 19. DTI of rotating model with mirror, 16 November 1976, tracked nose return.
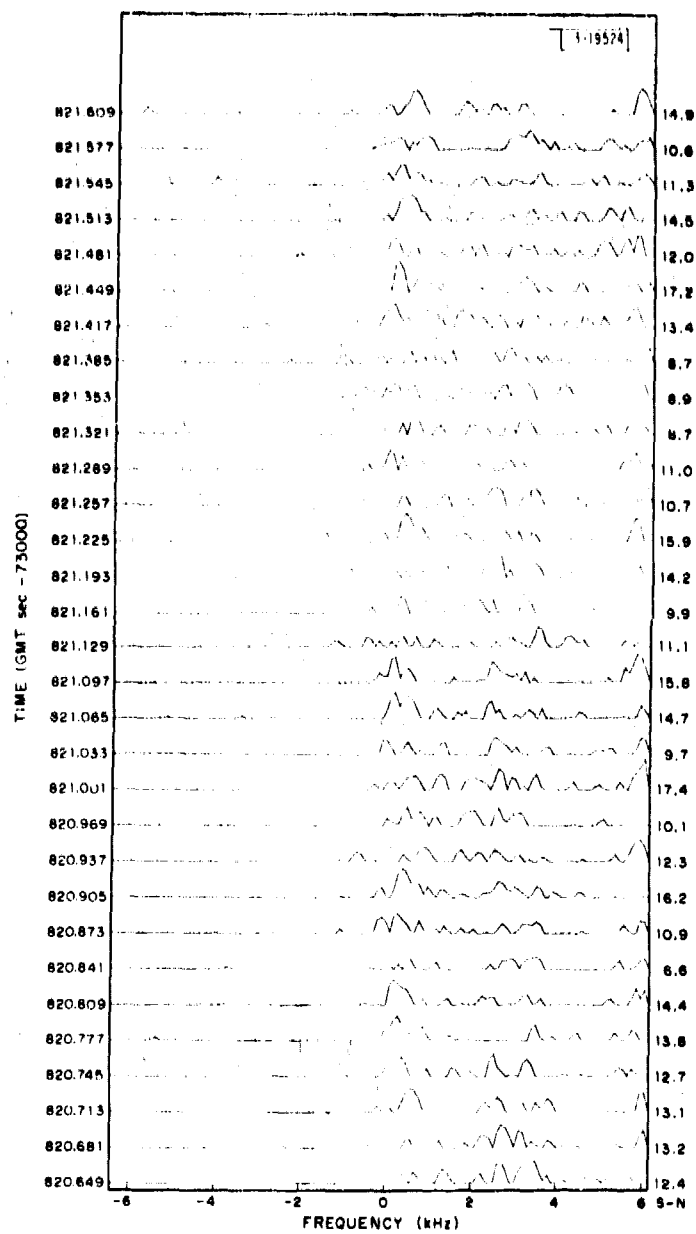
Fig. 20. Amplitude of Doppler spectrum, rotating model with mirror, 16 November 1976, tracked nose return.

17
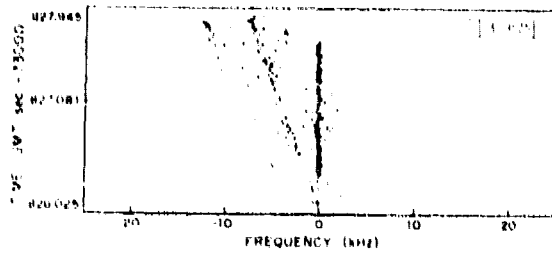
Fig. 21.   DTI of rotating model with mirror, 16 November 1976, tracked mirror return.
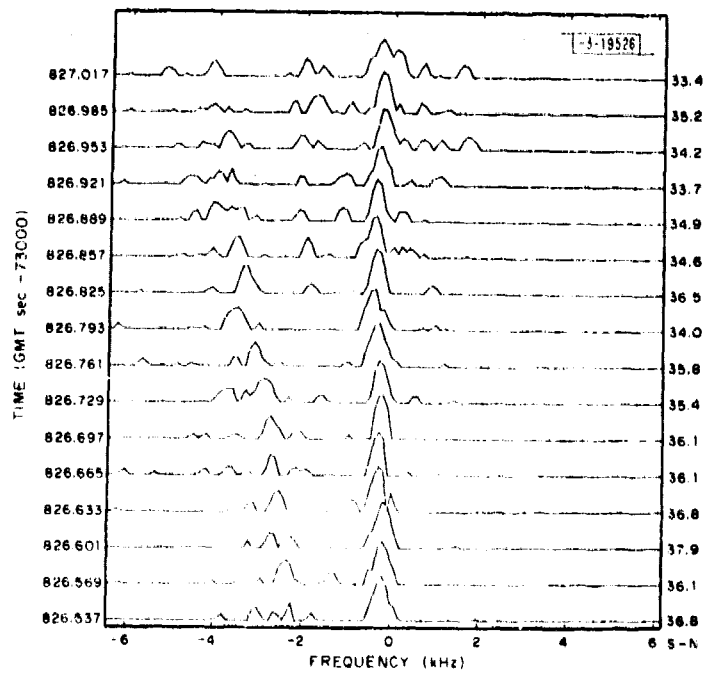
Fig. 22.   Amplitude of Doppler spectrum, rotating model with mirror, 16 November 1976, tracked mirror return.

18

Fig. 23. Components of peak mirror return, 16 November 1976.
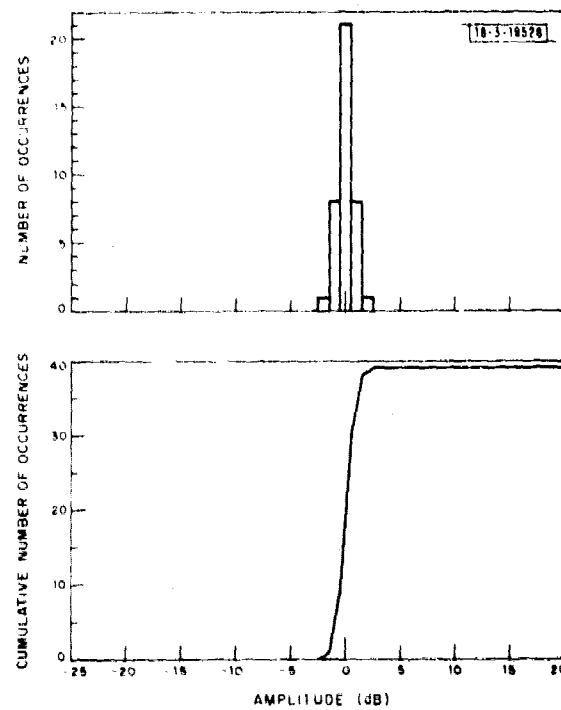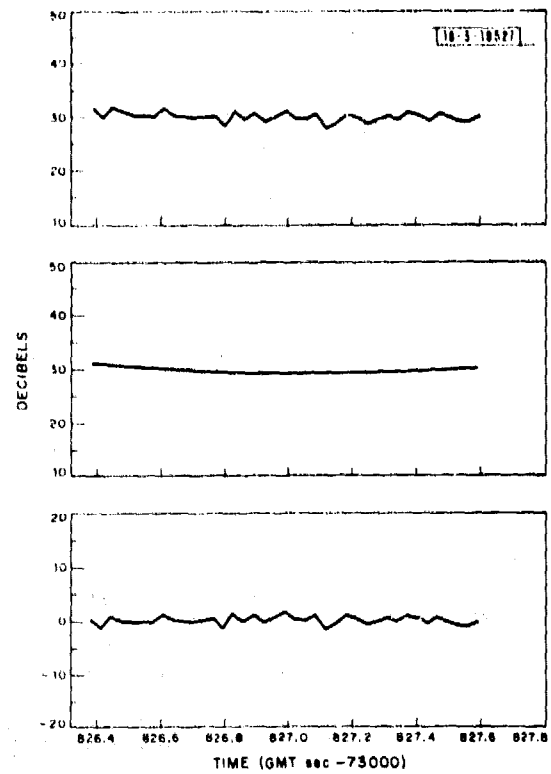
Fig. 24. Amplitude distribution of peak mirror return, 16 November 1976.

19

IV. FIVE-KM RANGE EXPERIMENT 14 DECEMBER 1976

A. Introduction

In the experiment of 16 November, the mirror return was present from approximately zero aspect to 9 deg after zero aspect. When the nose was in the same position, its return could not be separated from those of the other scatterers, hence the two returns could not be measured at the same position in the illuminating beam. The validity of any comparison between the nose and mirror returns would therefore depend on the uniformity of the illumination. A further experiment was conducted on 14 December which overcame this limitation by having the mirror mounted close to the nose and oriented so that its return would be seen at an angle at which the nose return could be easily separated.

B. Returns from Nose and Mirror

Figure 25 shows a section of the DTI from the experiment conducted on 14 December. The nose return is at the extreme left, with the short-duration strong mirror return to the right of it. These returns do not follow the expected smooth curves because of variation in the rate of rotation of the turntable. These variations were probably caused by wind forces acting on the model. The perturbations in the Doppler frequency precluded the extraction of a return in a single tracked cell, but did not prevent the peak amplitude in Doppler from being separated and analyzed.

The standard deviation of the high-frequency component of the nose return was found to be 2.5 dB, and is much the same as the values obtained from the previous experiments. The standard deviation of the mirror return was 1.1 dB, as compared to 0.8 dB for the returns obtained on 16 November. The difference between the amplitudes of the mirror and nose returns was 25 dB. This is the same as was obtained in the previous test, indicating that the illumination intensity had been substantially uniform on the earlier experiment.

V. SUMMARY AND DISCUSSION

A. Summary Table

Table I summarizes the measurements made. The rows of the table correspond to the individual feature measurements and are divided into sections corresponding to the experiments. Four of the columns correspond to the type of measurement performed. The first column gives the mean signal in the Doppler cell that gave the largest mean return, and column two gives the standard deviation of its high-frequency component. Columns three and four give the corresponding values for the peak signal in Doppler space. Columns five and six give the theoretical cross sections of specular and Lambertian spheres of the same radius as the nose. These have the same arbitrary reference as the other measurements and were scaled from the mirror returns recorded on the same experiment. The RCS of a specular sphere is equal to its physical cross section, while the RCS of a depolarizing Lambertian sphere is 1.25 dB higher. The derivation of these cross sections is given in Appendix I. The theoretical returns from the specular spheres shown in the table were obtained by scaling the returns from the mirror according to the radius squared. The returns from the hypothetical Lambertian sphere were obtained by adding 1.25 dB to those of the specular spheres.
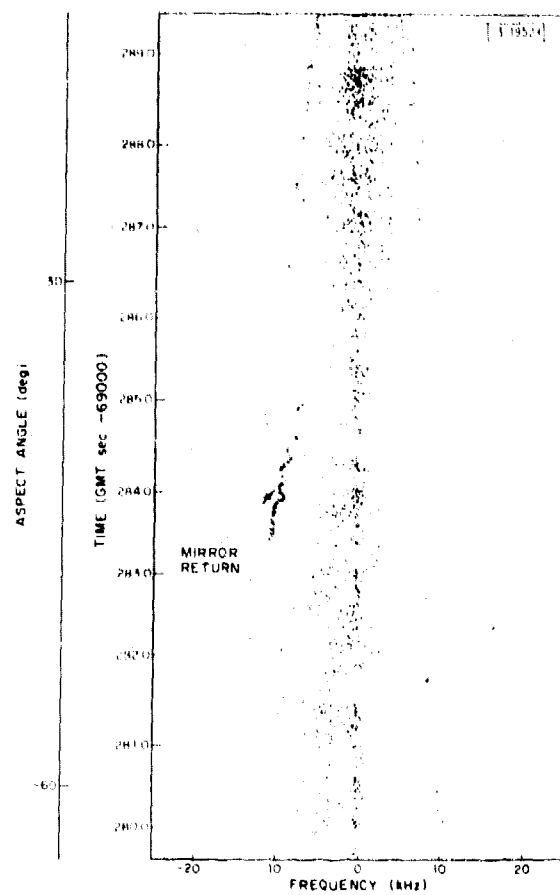
Fig. 25.   DTI of rotating model with mirror, 14 December 1976.

| | TABLE 1 | | | | | |
| | SUMMARY | | | | | |
	Single-cell mean (dB)	Single-cell standard deviation (dB)	Peak-cell mean (dB)	Peak-cell standard deviation (dB)	Specular mean (dB)	Lambertian mean (dB)
Nose 22 October 1976 Segment 1	−1.0	5.5	5.0	2.6		
Nose 22 October 1976 Segment 2	2.0	6.4	9.0	2.8		
Nozzle 22 October 1976 Segment 1			7.0	2.0		
Nozzle 22 October 1976 Segment 2			8.0	2.4		
Nose 16 November 1976	−3.0	6.0	5.0	2.7	8.1	9.3
Mirror 16 November 1976	28.0	3.1	30.0	0.8		
Nose 14 December 1976			2.0	2.5	5.0	6.2
Mirror 14 December 1976			27.0	1.1		
Noise		6.2				

B. RCS of Spherical Nose

It can be seen from the table that in both experiments where the sphere was used, the peak signal in Doppler from the nose was approximately 3.0 dB below the theoretical return from the specular sphere, and approximately 4.2 dB below that for a Lambertian sphere.

Other observations pertaining to the nose return that can be made from the table are given below.

(1) Taking the return in a single Doppler cell rather than the maximum return, resulted in an average drop in signal of 7.0 dB and an average increase in the standard deviation of the high-frequency component of 3.3 dB.

(2) The average standard deviation of the high-frequency component of the single-cell nose return was 6.0 dB. This is close to the value of 6.2 dB for a Rayleigh-distributed noise-type signal. The amplitude distributions of these returns are also similar to those of the noise signal.

C. Fluctuations in Mirror Return

The fluctuation in the return from the spherical mirror is attributed to atmospheric effects. Investigations into the propagation of optical beams in turbulent media have been reported by Lawrence and Stohbehn,[*] and Fante.[†] In these publications, the variable usually calculated is the variance of the natural logarithm of the intensity, σ_{lnI}^2, where intensity is a measure of power per unit area. This variable can be directly obtained from the standard deviation of the signal in decibels by multiplying by 0.23 and squaring. Thus the values of σ_{lnI}^2 corresponding to 0.8 and 1.1 dB standard deviation are 0.034 and 0.064, respectively. These figures apply to a two-way path. If there is no correlation between the fluctuations imposed on the outgoing and return paths, the variance for a one-way path will be half that for a two-way path. If there is total correlation, the one-way variance will be 0.25 times the two-way variance.

Lawrence and Strohbehn[*] give an expression for small values of σ_{lnI}^2 for a spherical wave in a locally isotropic, homogeneous random medium as follows:

$$\sigma_{lnI}^2 = 0.50 \ C_n^2 \ k^{7/6} \ l^{11/6}$$

where C_n^2 is the refractive-index structure parameter, k is 2π/wavelength, and L is the range to the target. Solving for C_n^2 and substituting for L and k gives,

$$C_n^2 = \frac{\sigma_{lnI}^2}{1.64 \times 10^{13}} \ .$$

For 0.8 dB standard deviation on a two-way path and no correlation, σ_{lnI}^2 for a one way path is 0.017. Then $C_n^2 = 1.03 \times 10^{-15}$ m$^{-2/3}$. For 1.1 dB standard deviation, $C_n^2 = 1.94 \times 10^{-15}$ m$^{-2/3}$. C_n^2 can vary from 10^{-17} or less for weak turbulence to 10^{-13} or more for strong turbulence. The turbulence existing during the experiments would be classed as moderate.

---

* R. Lawrence and J. Strohbehn, "A Survey of Clear-Air Propagation Effects Relevant to Optical Communications," Proc. IEEE 58, 1523-1545 (1970).

† R. Fante, "Electromagnetic Beam Propagation in Turbulent Media," Proc. IEEE 63, 1669-1689 (1975).

ACKNOWLEDGMENT

24

APPENDIX I
RADAR CROSS SECTIONS OF SPHERES

DEFINITION OF RADAR CROSS SECTION

Let β = bistatic angle

$$RCS(\beta) = \frac{4\pi}{D_i} F(\beta) Lp$$

where $F(\beta)$ is the power per unit solid angle scattered in the bistatic direction, D_i is the incident flux density per unit area, and Lp is a polarization loss factor which is a function of the target and receiver characteristics.

SCATTERING CHARACTERISTICS OF A SPECULAR SPHERICAL SURFACE

Let the range from the source to the target be much greater than a wavelength so that geometric optics approximation apply. Two cases are considered, the first when the surface is convex, and the second when it is concave. These are illustrated in Fig. I-1. Let α be the azimuthal angle of the normal to an element of area of a specular spherical surface of radius r. It is also the azimuthal angle of the direction of energy flow reflected from that element. Let Θ be the polar angle of the normal to the element of area. Θ is zero in the direction of the source. Let $\Theta_c(\alpha)$ be the polar angle at the periphery of the spherical surface. The element of area dA is given by,

$$dA = r^2 \sin\Theta \, d\Theta \, d\alpha \quad.$$

The power incident on dA is

$$dP_i = \begin{cases} D_i dA \cos\Theta = D_i r^2 \sin\Theta \cos\Theta \, d\Theta \, d\alpha & \text{for } \Theta < \Theta_c(\alpha) \\ 0 & \text{for } \Theta > \Theta_c(\alpha) \end{cases} \quad.$$

The direction of the reflected energy flow from this element of area is (β, α), where β is the polar angle of the reflected radiation.

$$\beta = 2\Theta, \quad d\beta = 2d\Theta \quad.$$

The element of solid angle in the reflected energy wave number space is:

$$d\Omega = \sin\beta \, d\alpha \, d\beta = \sin(2\Theta) \, d\alpha \, (2d\Theta)$$

$$= 4 \sin\Theta \cos\Theta \, d\Theta \, d\alpha \quad.$$

The power reflected into unit solid angle in the direction (β, α) is given by:

$$F_s(\beta, \alpha) = \frac{dP_i}{d\Omega} = \frac{D_i r^2 \sin\Theta \cos\Theta \, d\Theta \, d\alpha}{4 \sin\Theta \cos\Theta \, d\Theta \, d\alpha} = \frac{D_i r^2}{4} \quad.$$

---

* Authored by H. Jones.
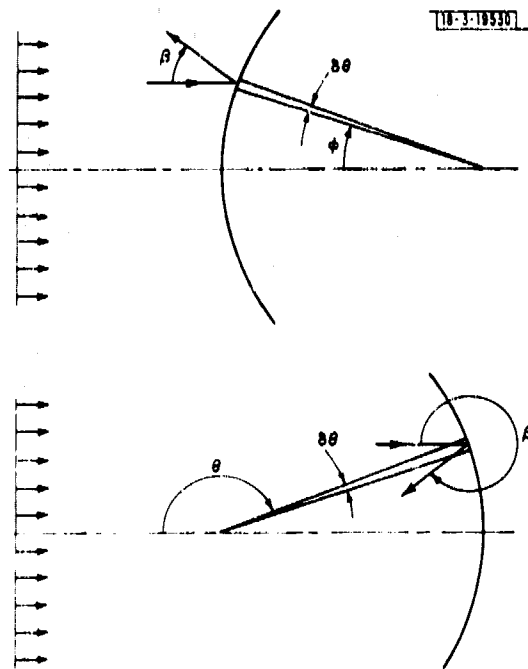
Fig. 1-1. Geometry of reflection from a specular spherical surface.

26

In the Firepond radar, the polarization of the detector is matched to the return from the specular sphere. The value of Lp is therefore unity. The bistatic cross section in the direction (β, α) is

$$RCS(\beta, \alpha) = \frac{4\pi \, F_s(\beta, \alpha) \, Lp}{D_i} \quad \begin{cases} \pi r^2 & \text{for } 0 < \theta_\epsilon(\alpha) \\ 0 & \text{for } 0 > \theta_\epsilon(\alpha) \end{cases} .$$

For a convex specular sphere, if $\theta_\epsilon(\alpha)$ is equal to or greater than $\pi/2$ for all values of α, then the RCS is independent of α and β. Thus a specular sphere is an isotropic scatterer with RCS equal to its geometric cross section. For a concave specular spherical surface, if $\theta_\epsilon(\alpha)$ is equal to or greater than $\pi/4$, multiple reflections can occur and the RCS might differ from that given by the expression above.

LAMBERTIAN SCATTERING FROM AN ELEMENTAL AREA

Let F_ℓ be the scattered power flux from an element of area. If the total scattered power from this area is P_s, then

$$P_s = \int F_\ell \, d\Omega$$

where Ω denotes a solid angle.

The defining property of a Lambertian surface is that, regardless of the direction(s) of the incident radiation,

$$F_\ell(\varphi) = \begin{cases} F_\ell(0) \cos \varphi & \text{for } \varphi < \pi/2 \\ 0 & \varphi > \pi/2 \end{cases}$$

where φ is the angle between the direction of emission and the normal to the element of area.

Calculation: To obtain $F_\ell(0)$ in terms of P_s.

$$P_s = \int F_\ell(\varphi) \, d\Omega$$

$$\begin{cases} F_\ell(\varphi) = \begin{cases} F_\ell(0) \cos \varphi & \text{for } \varphi < \pi/2 \\ 0 & \text{for } \varphi > \pi/2 \end{cases} \\ d\Omega = \sin \varphi \, d\alpha \, d\varphi \end{cases}$$

where α is the azimuthal direction.

$$P_s = F_\ell(0) \int_{\varphi=0}^{\pi/2} \int_{\alpha=0}^{2\pi} \cos \varphi \sin \varphi \, d\alpha \, d\varphi$$

$$= 2\pi \, F_\ell(0) \int_0^{\pi/2} \sin \varphi \cos \varphi \, d\varphi$$

$$= 2\pi \, F_\ell(0) \int_{\varphi=0}^{\pi/2} d(\sin^2 \varphi)/2$$

$$= \pi F_\ell(0) \quad .$$

Therefore

$$F_\ell(0) = \begin{cases} P_s \cos \varphi/\pi & \text{for } \varphi < \pi/2 \\ 0 & \text{for } \varphi > \pi/2 \end{cases} \quad .$$

Therefore $F_\ell(\varphi)$ total power scattered, times the cosine of the angle away from the normal, divided by π.

MONOSTATIC RCS OF A LAMBERTIAN SPHERE

Let α be the azimuthal angle of the normal to the element of area dA on a Lambertian sphere of radius r, and Θ the polar angle, then

$$dA = r^2 \sin\Theta \, d\Theta \, d\alpha \quad .$$

The power incident on dA is assumed to be equal to the power scattered, that is, the surface is "white" rather than "grey," thus,

$$dP_i = dP_s = D_i \cos\Theta \, dA = D_i r^2 \sin\Theta \cos\Theta \, d\Theta \, d\alpha \quad .$$

The scattered flux per unit solid angle in the direction of the receiver from this element of area, is given by

$$dF_\ell = dP_s \cos\Theta/\pi = D_i r^2 \sin\Theta \cos^2\Theta \, d\Theta \, d\alpha/\pi$$

since $\Theta = 0$ in this monostatic case. Integrating over the illuminated hemisphere gives the total flux per unit solid angle at the receiver.

$$F_\ell(0) = \int_{\Theta=0}^{\pi/2} \int_{\alpha=0}^{2\pi} dF = \frac{D_i r^2}{\pi} (2\pi)(-1/3) \int_{\Theta=0}^{\pi/2} d(\cos^3\Theta)$$

$$= 2/3 \, r^2 D_i \quad .$$

The return from a Lambertian surface is randomly polarized, so on the average, the power detected by the polarization sensitive receiver is half the total power received. Thus Lp has a value of 0.5. The monostatic RCS is

$$RCS_\ell(0) = \frac{4\pi F_\ell(0) \, Lp}{D_i} = 4/3\pi r^2 \quad .$$

This exceeds the specular sphere RCS by the factor 4/3 or 1.25 dB.

An examination of the more complicated integral for $\beta \neq 0$, shows that for the Lambertian sphere, the bistatic RCS decreases monotonically to zero as β increases to π. Thus the increased monostatic RCS of the Lambertian sphere is not inconsistent with the fact that it intercepts the same total energy as the specular sphere.

28

REPORT DOCUMENTATION PAGE		READ INSTRUCTIONS BEFORE COMPLETING FORM
1. REPORT NUMBER ESD-TR-77-111	2. GOVT ACCESSION NO.	3. RECIPIENT'S CATALOG NUMBER
4. TITLE (and Subtitle) Analysis of Firepond IR RCS Data on Rocket Model		5. TYPE OF REPORT & PERIOD COVERED Project Report
		6. PERFORMING ORG. REPORT NUMBER
7. AUTHOR(s) Bruce A. Francis		8. CONTRACT OR GRANT NUMBER(s) F19628-76-C-0002
9. PERFORMING ORGANIZATION NAME AND ADDRESS Lincoln Laboratory, M.I.T. P. O. Box 73 Lexington, MA 02173		10. PROGRAM ELEMENT, PROJECT, TASK AREA & WORK UNIT NUMBERS ARPA Order 600 Program Element 62301E Project No. 6E20
11. CONTROLLING OFFICE NAME AND ADDRESS Defense Advanced Research Projects Agency 1400 Wilson Boulevard Arlington, VA 22209		12. REPORT DATE 18 May 1977
		13. NUMBER OF PAGES 34
14. MONITORING AGENCY NAME & ADDRESS (if different from Controlling Office) Electronic Systems Division Hanscom AFB Bedford, MA 01731		15. SECURITY CLASS. (of this report) Unclassified
		15a. DECLASSIFICATION DOWNGRADING SCHEDULE

16. DISTRIBUTION STATEMENT (of this Report)

Approved for public release; distribution unlimited.

17. DISTRIBUTION STATEMENT (of the abstract entered in Block 20, if different from Report)

18. SUPPLEMENTARY NOTES

None

19. KEY WORDS (Continue on reverse side if necessary and identify by block number)

infrared radar
scale model rocket body
rotating model experiments

Doppler-Time-Intensity display
radar cross sections of spheres

20. ABSTRACT (Continue on reverse side if necessary and identify by block number)

Coherent narrowband infrared radar returns from a fixed rotating target were analyzed. The data were taken using the Firepond radar facility with small-aperture transmitting and receiving antennas at a range of 5 km. The amplitude distribution of the returns from the target were compared with those from a spherical mirror.

DD FORM 1473 EDITION OF 1 NOV 65 IS OBSOLETE
1 JAN 73